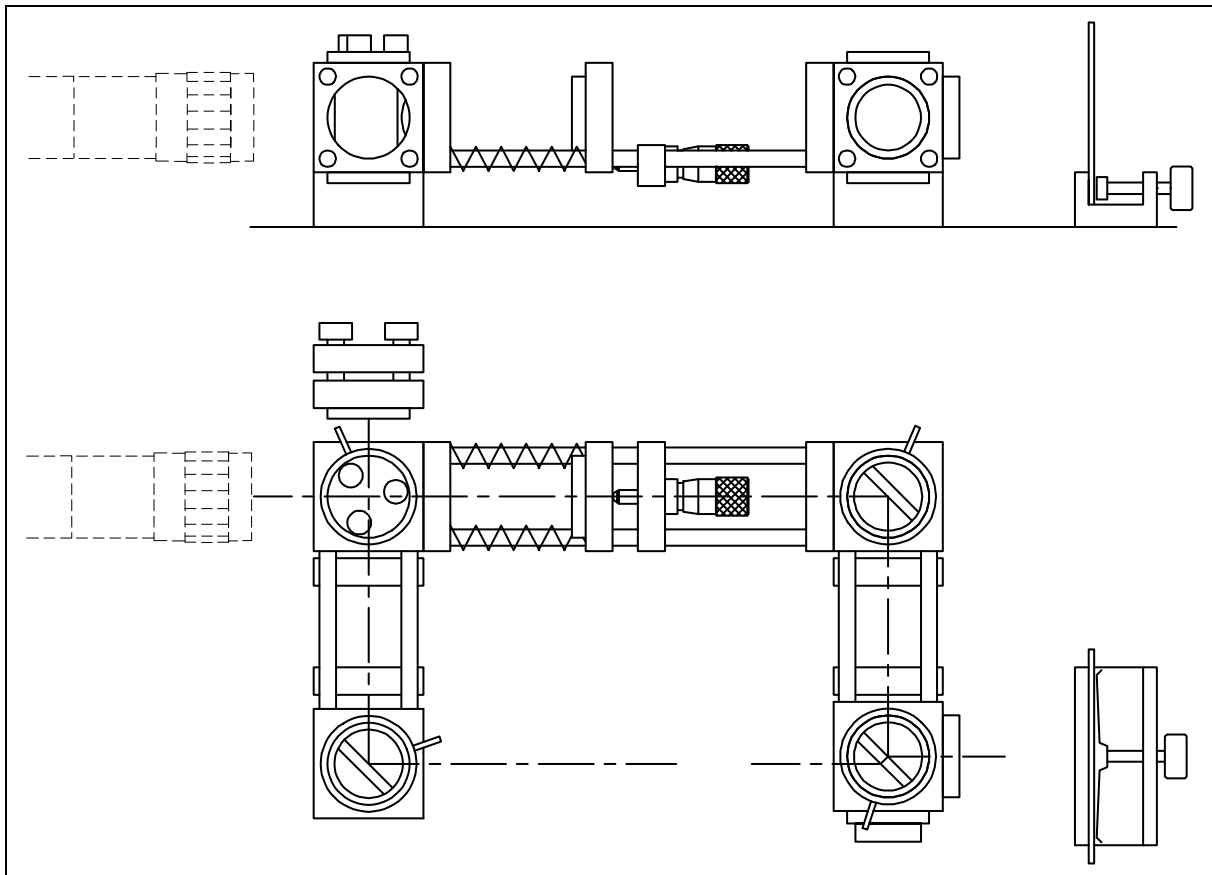


# LABORATORY MANUAL

## TWO-BEAM INTERFEROMETERS



Laboratory manual prepared by Prof. Dr. F. Mohr,  
Department of Engineering Physics, Metrology, and Precision Engineering,  
Fachhochschule Hildesheim-Holzminde, Germany

# TWO-BEAM INTERFEROMETERS

<b>1 Introduction</b>	<b>3</b>
<b>2 Basic Concepts</b>	<b>3</b>
2.1 Wave Nature of Light	3
2.2 Phase Velocity and Refractive Index	4
2.3 Complex Representation of Electric Fields	4
2.4 Intensity	4
<b>3 Optical-Interference Phenomena</b>	<b>5</b>
3.1 Two-Beam Interference	5
3.2 Interference Fringes and Rings	6
3.3 Interference of Monochromatic and White Light	8
<b>4 Optical Interferometers</b>	<b>9</b>
4.1 Mach-Zehnder and Michelson Interferometers	9
4.2 Michelson and Twyman-Green Interferometers	9
<b>5 Application Notes</b>	<b>10</b>
5.1 Assembling the Experimentation Kit	10
5.2 Simple Experiments with the Michelson Interferometer	11
5.2.1 Initial Alignment	11
5.2.2 Interferometric Studies of the Thermal Expansion of Test Samples	12
5.3 Mach-Zehnder Interferometers	12
5.3.1 Conversion to a Mach-Zehnder Interferometer	12
5.3.2 Determining Refractive Indices with a Mach-Zehnder Interferometer	13
5.4 Checking Glass Slides with a Twyman-Green Interferometer	13
<b>6 Bibliography</b>	<b>13</b>
<b>7 Assembly Drawings and Photographs</b>	<b>14</b>
7.1 Component Modules	14
7.2 Photograph of the Fully Assembled Two-Beam Interferometer	14
7.3 Assembly Drawing	15
<b>8 Components List</b>	<b>16</b>

## 1 Introduction

Numerous physical phenomena may be explained in terms of waves. Examples include the propagation of radio signals or light, both of which are electromagnetic waves, the latter at optical frequencies. Waves interfere when superimposed. Interference occasionally obscures effects of interest, but is frequently intentionally caused in order to allow high-precision measurements of physical quantities, such as length, distance, angle, speed, surface figure, planarity, parallelism, or related physical quantities, in terms of the differences in optical paths of several (two in the cases to be considered here) light beams of known, identical, wavelength, where their wavelength thus constitutes the metric standard.

Alternatively, optical interferometers of known physical dimensions may be used to determine the wavelengths of light emitted by monochromatic sources or to accurately analyze the emission spectra of white-light sources.

The interferometers to be described here, all of which may be assembled from Linos Photonics microbench components, are suitable for use in both studies of two-beam interference phenomena and high-precision metrology, although the latter may require use of additional components.

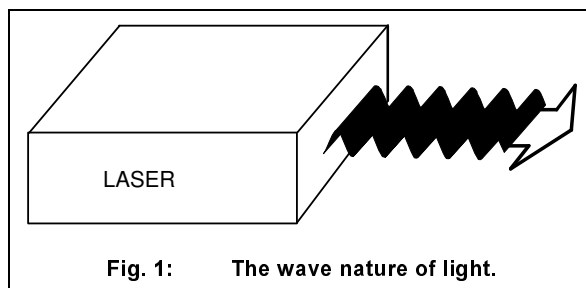
We discuss below the fundamental principles of two-beam interferometry, the basic types of two-beam interferometers assemblable from Linos Photonics microbench components, concluding with discussions of several typical applications.

## 2 Basic Concepts

### 2.1 Wave Nature of Light

Optical-interference phenomena are due to the wave nature of light. Fig. 1 depicts a collimated light beam emitted by a laser as a traveling wave. Unlike waves propagating on the surfaces of liquids or solids, which has been taken as a model here, light waves are periodically varying electromagnetic fields propagating through space rather than undulatory motions of material media.

For our purposes, we may regard traveling light waves as periodically varying electric fields propagating along the z-



axis, with  $E$ , the electric field at spatial coordinate  $z$  at time  $t$ , given by

$$E = E(z, t) = \hat{E} \cdot \cos(kz - \omega t) . \quad (1)$$

where  $\hat{E}$  is the field's peak value, or amplitude, and  $k$  and  $\omega$  will be defined below. Fig. 2 schematically depicts propagation of the wave train of Eq. 1 in greater detail, where  $a$ ,  $b$ , and  $c$  represent consecutive stages in its emission by a source, as viewed normal to the direction of propagation, and the wave is shown as a periodic train of crests and valleys exiting the source.

Plotting temporal variations in electric field, indicated by 1, 2, and 3 in Fig. 2, at a given point along the wave's propagation axis rather than taking "time-lapse" photographs of its spatial distribution at various times, as in  $a$ ,  $b$ , and  $c$ , yields the periodic variation in electric field shown in Fig. 2d.

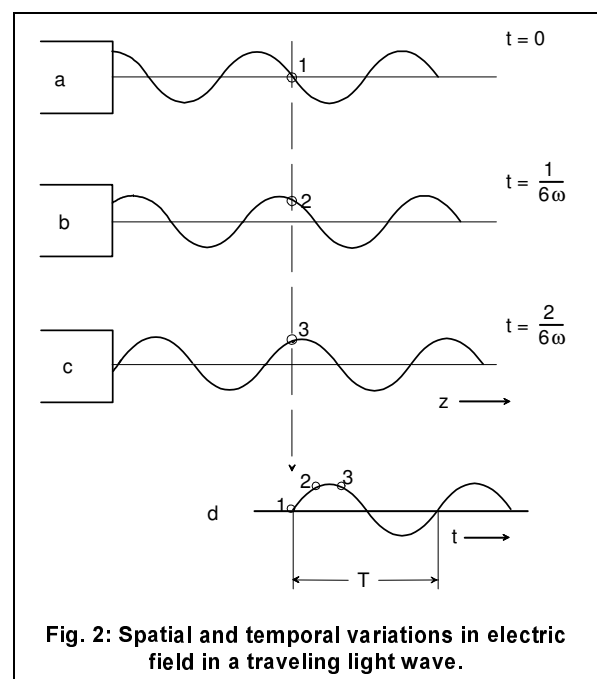
The temporal period,  $T$ , of this wave is

$$T = 1/\omega = 2\pi/\nu , \quad (2a)$$

where  $\omega$  is its frequency, which for visible light will be of order  $10^{14}$  Hz, and  $\omega$  is its "angular frequency." Photo-detectors are incapable of responding to such high frequencies, and thus yield only time-averaged intensities (cf. Section 2.4, below).

The wave's spatial period, or "wavelength,"  $\lambda$ , is related to its "angular wavenumber," or "propagation constant,"  $k$ , by

$$\lambda = 2\pi/k . \quad (2b)$$



## 2.2 Phase Velocity and Refractive Index

In Eq. 1, the argument of the cosine function,

$$kz - \omega t \equiv \phi_i(z, t) \quad (3a)$$

is the wave's instantaneous phase. Eq. 3a will be satisfied at all points along the wave train where the electric field has a given, fixed, value. Eq. 3a thus correlates  $z$  and  $t$ . For wave crests,  $\phi_i = 0$ , since the electric field has its maximum value,  $\hat{E}$ , when the cosine function has its maximum value of unity. Thus, at wave crests

$$kz - \omega t = 0. \quad (3b)$$

Solving this equation for the spatial coordinate,  $z$ , we find that wave crests occur at points where

$$z = \frac{\omega}{k} \cdot t. \quad (4)$$

The speed at which wave crests propagate is thus

$$c = \frac{dz}{dt} = \frac{\omega}{k} = \lambda \cdot \nu. \quad (5a)$$

This speed,  $c$ , is termed the wave's "phase velocity," since it represents the speed at which points of constant phase, in this case,  $\phi_i = 0$ , propagate. Note that the relation of Eq. 5a holds for any chosen value of  $\phi_i$ , and not merely for the special case  $\phi_i = 0$ . This "phase velocity,"  $c$ , is thus commonly referred to as "the speed of light."

The time-independent term of Eq. 1 is called the wave's "initial phase," its phase at time  $t = 0$ ,  $\phi_0$ . The subscript is normally omitted, yielding simply  $\phi$ , which is thus given by:

$$\phi = kz. \quad (6)$$

From the classical theory of electromagnetic fields, we know that light waves transiting material media have phase velocities varying with the media involved. Eq. 5a thus holds only in vacuum, and must be modified by inserting a "refractive index,"  $n$ , characterizing the medium involved, in all other cases. For light propagating in material media, Eq. 5a thus becomes

$$c_n = \frac{c}{n} = \frac{\omega}{n \cdot k_0} = \frac{\lambda_0}{n} \cdot \nu. \quad (5b)$$

where  $k_0$  and  $\lambda_0$  are the vacuum values of propagation constant and wavelength, respectively. Since the frequencies of light waves are entirely determined by the characteristics of their sources, they are unaffected by the properties of transmitting media. Equating the frequencies appearing in Eqs. 5a and 5b, we thus find that the propagation constants and wavelengths of light waves in material media are related to their vacuum values by

$$k = n \cdot k_0 \quad \text{and} \quad \lambda = \frac{\lambda_0}{n}. \quad (7a, 7b)$$

The "initial phase,"  $\phi$ , defined in Eq. 6, also requires re-definition. We may allow for the characteristics of transmitting media by setting

$$\phi = nk_0 \cdot z = 2\pi \cdot \frac{n}{\lambda_0} \cdot z. \quad (8)$$

Light waves traversing material media will thus be shifted in phase,  $\phi$ , by amounts proportional to both the refractive indices,  $n$ , of the media involved and the physical lengths,  $z$ , of paths they traverse within media. This fact is utilized in interferometric refractometry, as well as in other fields.

## 2.3 Complex Representation of Electric Fields

We have thus far represented traveling light waves in terms of simple trigonometric functions, as in Eq. 1. Experience shows that this leads to rather cumbersome mathematical expressions in cases involving extensive computations. Using complex representation yields much more readily handled expressions. Substituting its complex equivalent for the cosine in Eq. 1, we obtain

$$E = \hat{E} \cdot \text{Re} \left\{ e^{-i(\omega t - kz)} \right\}. \quad (9)$$

where  $\text{Re}\{\zeta\}$  indicates the real part of an arbitrary complex number,  $\zeta$ . Eq. 9 thus simplifies to  $\text{Re} \{ e^{-i(\omega t - kz)} \} = \text{Re} \{ \cos(\omega t - kz) - i \sin(\omega t - kz) \} = \cos(\omega t - kz)$ . The notation of Eq. 9 is commonly employed in treating wave phenomena, but the "Re" is normally omitted, with the understanding that physical electric fields are represented entirely by their real parts. A further benefit of using complex representation is that it allows separating the spatial and temporal variations of electric fields and expressing them in the form

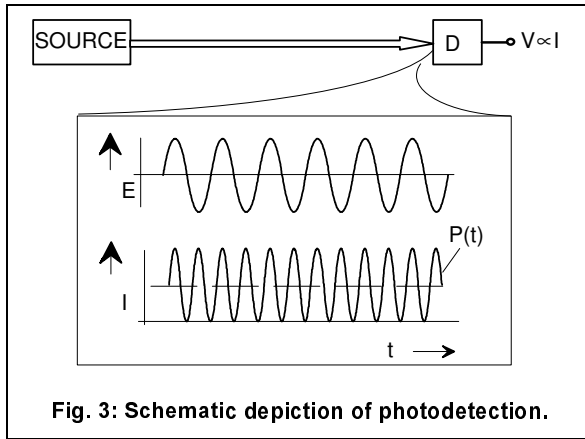
$$E = \hat{E} \cdot e^{ikz} \cdot e^{-i\omega t} = \hat{E} \cdot e^{i\phi} \cdot e^{-i\omega t}, \quad (10)$$

which, according to the foregoing discussion, is equivalent to Eq. 1.

## 2.4 Intensity

In attempting to detect light waves, one encounters a problem that does not arise for much lower-frequency electromagnetic waves, such as radio waves: available detection media are incapable of responding to the very high-frequency electric fields of light waves. Fig. 3's depiction of a detector responding to the temporal variations in electric field,  $E$ , of a light wave is thus misleading. The lower waveform, that of instantaneous radiant power,  $I$ , has angular frequency  $2\omega$ , twice that of the electric field, is thus also undetectable.

All available photodetectors, such as the human eye, photodiodes, photomultiplier tubes, photographic film, etc., respond to time-averaged radiant power,  $P$ , only. However, radiant power density, i.e., radiant power incident on unit area, or "intensity,"  $I$ , rather than  $P$ , is normally measured in interferometry. The case of con-



**Fig. 3: Schematic depiction of photodetection.**

stant intensity is indicated by the dotted line in Fig. 3. Intensity,  $I$ , is defined as the squared modulus of the electric field, or

$$I = |E|^2 = E \cdot E^* \quad (11)$$

where  $E^*$  is the complex conjugate of the electric field,  $E$ . The intensity,  $I$ , incident on a detector,  $D$ , will be converted into a voltage,  $V$ , proportional to  $I$ , as indicated in Fig. 3.

It should be noted that although in Section 2.1 the light source discussed was a laser, all statements made above, as well as treating light as electromagnetic waves, apply to light from any source, including conventional lamps.

### 3 Optical-Interference Phenomena

#### 3.1 Two-Beam Interference

We will now proceed to discuss interference phenomena based on the equations derived above and the experimental setup schematized in Fig. 4, which depicts a light beam from a source being split into two beams. The beam exiting the source, which has intensity  $I_0$ , strikes a beamsplitter, i.e., a partially transmitting/partially reflecting mirror, BS1, where it is split into two beams, each having half the intensity of the incident beam. Each of these two beams is deflected through  $90^\circ$  by one of the high-reflectance mirrors, M1 or M2, and then continues onward to a second beamsplitter, BS2, which subjects each beam to a further partial transmission/reflection. There are thus a total of four beam paths leading from the source,  $S$ , to one of the two detectors,  $D1$  or  $D2$ , namely

$$\begin{aligned} S \rightarrow BS1 \rightarrow M1 \rightarrow D1, \\ S \rightarrow BS1 \rightarrow M1 \rightarrow D2, \\ S \rightarrow BS1 \rightarrow M2 \rightarrow D1, \text{ and} \\ S \rightarrow BS1 \rightarrow M2 \rightarrow D2. \end{aligned}$$

Assuming a beamsplitting ratio of 50/50 for both BS1 and BS2, we find that  $2 \times 25\% = 50\%$  of source intensity,  $I_0$ ,

reaches  $D1$  and  $2 \times 25\% = 50\%$ , i.e., precisely this same intensity, also reaches  $D2$ , or so cursory inspection of Fig. 4 would seem to indicate.

However, the intensity detected by  $D1$  will depend on the relative phases of the two incident beams. If, for example, they arrive at  $D1$  precisely in phase, their amplitudes will add, i.e., they will interfere constructively, producing the maximum intensity attainable at  $D1$ . If they arrive at  $D1$  precisely one-half wavelength out of phase, their electric fields will be equal but of opposite sign and will cancel one another, i.e., will interfere destructively, and the intensity incident on  $D1$  will be zero. In either case, and in all intermediate cases, the intensity incident on  $D2$  will be equal to  $I_0$  less that incident on  $D1$ .

Mathematically, the electric field,  $E_{1a}$ , reaching  $D1$  via the upper of the two paths,  $a$ , may be written as

$$E_{1a} = r \cdot e^{i\phi_a} \cdot t \cdot E_0 \quad (12)$$

where  $r$  is the electric-field reflectance and  $t$  the electric-field transmittance of the two (identical) beamsplitters, BS1 and BS1, and  $E_0$  is the electric field of the beam exiting the source ( $|E_0| = \sqrt{I_0}$ ). Similarly, the electric field,  $E_{1b}$ , reaching  $D1$  via the lower of the two paths,  $b$ , may be written as

$$E_{1b} = t \cdot e^{i\phi_b} \cdot r \cdot E_0 \quad (13)$$

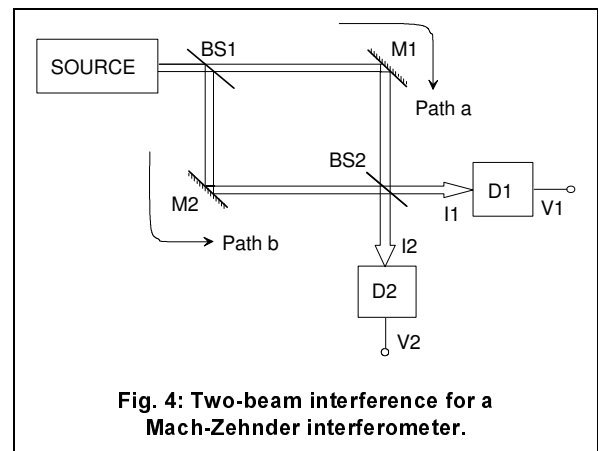
In Eqs. 12 and 13, the pathlengths of the two interfering beams enter through their respective phases,  $\phi_a$  and  $\phi_b$ . The resultant electric field at  $D1$  is the algebraic sum of the two interfering fields of Eqs. 12 and 13, or

$$E_1 = E_{1a} + E_{1b} = r \cdot t \cdot E_0 \cdot (e^{i\phi_a} + e^{i\phi_b}) \quad (14)$$

The intensity,  $I_1$ , incident on  $D1$ , will thus be given by

$$I_1 = |E_1|^2 = |r|^2 \cdot |t|^2 \cdot |E_0|^2 \cdot [e^{i\phi_a} + e^{i\phi_b}] \cdot [e^{-i\phi_a} + e^{-i\phi_b}] \quad (15)$$

Combining and simplifying the expressions in brackets, substituting  $I_0$  for  $|E_0|^2$ , letting  $|r|^2 = |t|^2 = 0.5$  (since



**Fig. 4: Two-beam interference for a Mach-Zehnder interferometer.**

we have assumed that BS1 and BS2 are both 50/50 beamsplitters), and defining

$$\Delta\phi = \phi_a - \phi_b \quad (16)$$

we ultimately obtain

$$I_1 = \frac{I_0}{2} \cdot (1 + \cos \Delta\phi) = I_0 \cdot \cos^2 \frac{\Delta\phi}{2} \quad (17a)$$

From conservation of energy, the intensity,  $I_2$ , at D2 must be equal to  $I_0$  less  $I_1$ , or

$$I_2 = \frac{I_0}{2} \cdot (1 - \cos \Delta\phi) = I_0 \cdot \sin^2 \frac{\Delta\phi}{2} \quad (17b)$$

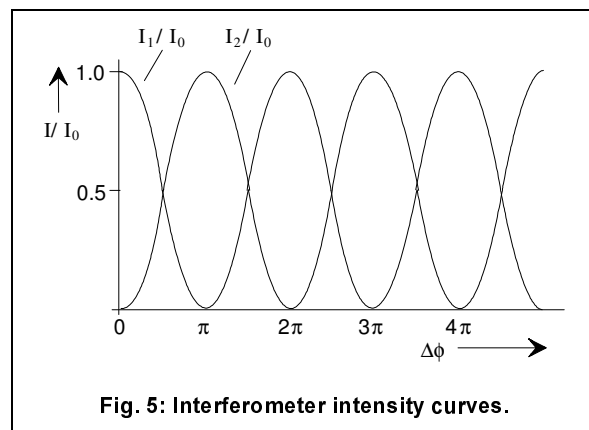
Plotting Eqs. 17a and 17b yields the intensity curves at the two detectors,  $I_1$  and  $I_2$ , for typical two-beam interferometers shown in Fig. 5, which are referred to as the interferometer's "interference functions."

Fig. 5 indicates that for a perfectly symmetric setup (i.e., for  $\Delta\phi = 0$ ), the full intensity of the source,  $I_0$ , will be detected at D1, i.e.,  $I_1$  will equal  $I_0$ , while no intensity will be detected at D2, i.e.,  $I_2 = 0$ . Lengthening one of the two paths to introduce a non-zero phase difference,  $|\Delta\phi| > 0$ , causes  $I_1$  to drop to zero while  $I_2$  rises from zero to a maximum of  $I_0$ . Continuing this lengthening causes  $I_1$  to rise while  $I_2$  drops, in accordance with the cosine relations of Eqs. 17a and 17b. This behaviour will be periodically repeated as path difference is further increased.

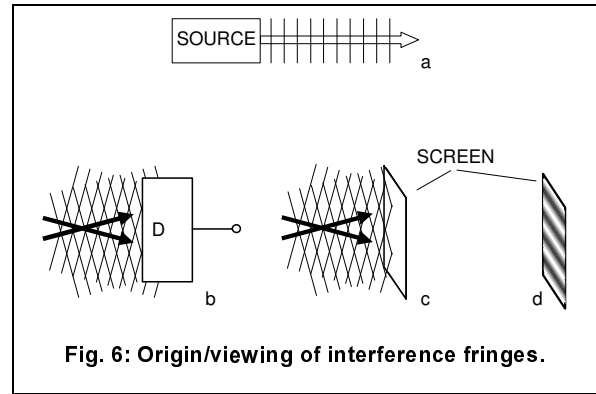
### 3.2 Interference Fringes and Rings

We have thus far implicitly presumed that interfering beams incident on viewing screens or detectors are perfectly coaxially aligned, i.e., that their wavefronts, or surfaces of constant phase, are accurately mutually parallel. Regarding wavefronts, cf. Figs. 1 and 6a, the latter of which depicts light waves emitted by a source, as viewed from above the source, where the parallel vertical lines represent propagating wavefronts.

Interference patterns will have identical phase differences, and thus uniform intensities, over the full photosensitive areas of detectors, only in the ideal case where interfering



**Fig. 5: Interferometer intensity curves.**



**Fig. 6: Origin/viewing of interference fringes.**

beams incident on detectors are perfectly coaxial. Obtaining uniform intensities over the full photosensitive areas of detectors further presumes that both interfering beams have uniform electric-field distributions transverse to their direction of travel, i.e., that both propagate as plane waves, a fact that should be mentioned at this point, but will not be discussed in detail.

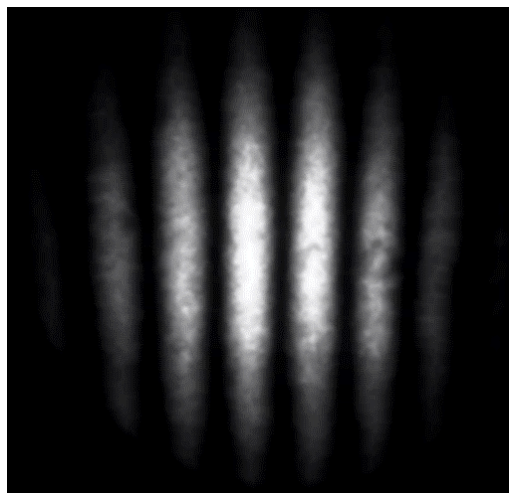
The requirement of perfectly coaxial alignment of interfering beams mentioned above will not always be readily achievable in actual practice. In many cases, interfering beams may even be intentionally misaligned such that wavefronts intersect at oblique angles, as shown in Figs. 6b and 6c.

Oblique intersection of wavefronts produces nonuniform intensity distributions over the photosensitive areas of detectors (Fig. 6b) or viewing screens (Fig. 6c). Since in this case the lines representing wave crests/valleys, or wavefronts, intersect only at certain discrete points, interference maxima/minima occur only at these points. These points of intersection are spread over the surfaces of detectors/viewing screens, resulting in the alternately bright/dark array of vertical bars shown in Fig. 7. Such interference patterns are termed "interference fringes." Fringe spacing, which corresponds to a phase difference of  $2\pi$ , will decline, i.e., fringes will become more closely spaced, as the angle between interfering wavefronts is increased. The case of parallel wavefronts described earlier thus represents the limiting case of infinite fringe spacing. Altering the phase difference,  $\Delta\phi$ , of interfering wavefronts thus causes interference fringes to "march" across the surfaces of detectors/viewing screens.

The interference fringes shown in Fig. 7 were obtained using the two-beam Michelson interferometer to be described in Section 4.1, below. Linos Photonics's Model 260 SW CCD-camera (Part No. 43 0060/43 0061) and "Vision2" image-processing system (Part No. 43 0100) were used to record this fringe pattern. Fig. 8 depicts its intensity distribution, obtained using the "Vision2"-system's three-dimensional plotting software.

In optical-interference experiments, particularly those employing lasers as light sources, electric fields of

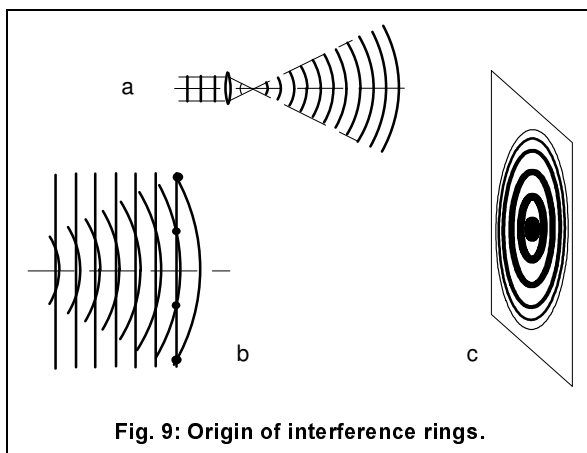




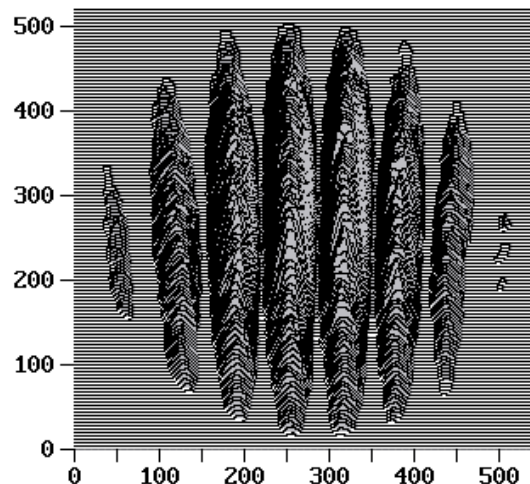
**Fig. 7: Interference fringes.**

interfering beams vary both longitudinally and laterally such that their wavefronts represent segments of spherical surfaces, or "spherical waves," rather than the plane waves we have been considering. The origination of spherical waves is schematically depicted in Fig. 9a, which shows light waves expanding from the focal point of a lens. It should be obvious from Fig. 9b that superimposing spherical wavefronts and plane wavefronts results in interference patterns consisting of concentric circular interference fringes, or rings, as shown in Fig. 9c. Interference fringe patterns of all types are generally termed "interferograms."

In two-beam interference experiments, both interfering beams are usually spherical waves, rather than plane waves or a plane wave and a spherical wave. From Fig. 9b, it can readily be inferred that interference of two spherical waves also yields concentric ring patterns, provided that their wavefronts have differing radii of curvature. This will nearly always be the case, since interfering beams will most likely have traversed differing optical pathlengths before interfering. The diameters and spacings of interference rings may be adjusted by



**Fig. 9: Origin of interference rings.**

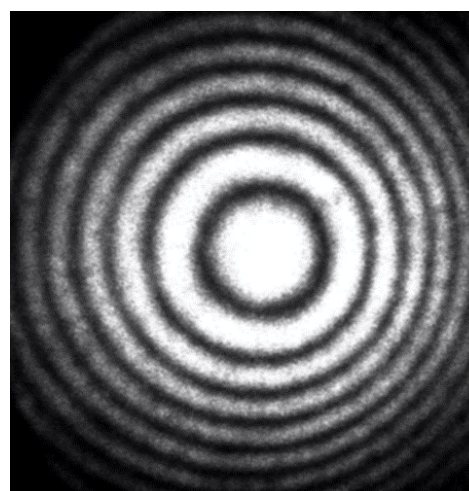


**Fig. 8: Intensity distribution for an interference-fringe pattern.**

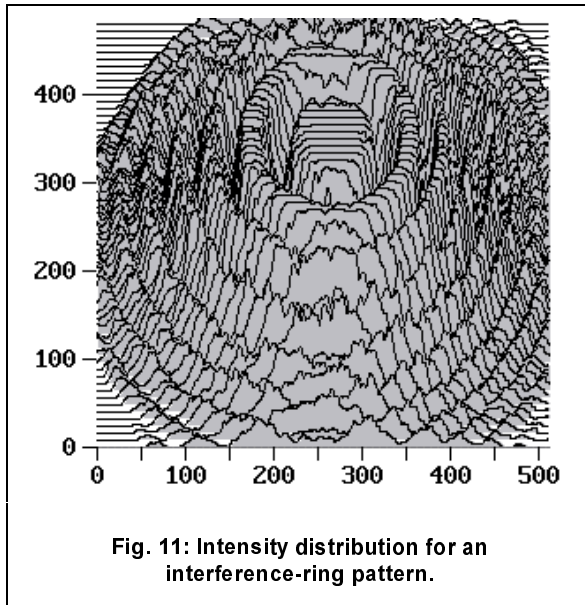
inserting optical elements, such as lenses or spherical mirrors, that alter beam convergence/divergence, into one or both beam paths.

Fig. 10 depicts interference rings generated using the two-beam Michelson interferometer to be described in Section 4.1. Fig. 11 shows the resulting intensity distribution, where peak intensities have been truncated for better clarity. Figs. 10 and 11 were obtained using the same equipment and software used to obtain Figs. 7 and 8.

In the most general case, interfering wavefronts will intersect at non-zero angles, and may also be laterally shifted. The interference fringes observed will then be off-axis segments of their total interference pattern. Virtually any desired interference pattern may be obtained if one understands the physics involved and utilizes suitable angular-alignment fixtures on optical components.



**Fig. 10: Interference rings.**



**Fig. 11: Intensity distribution for an interference-ring pattern.**

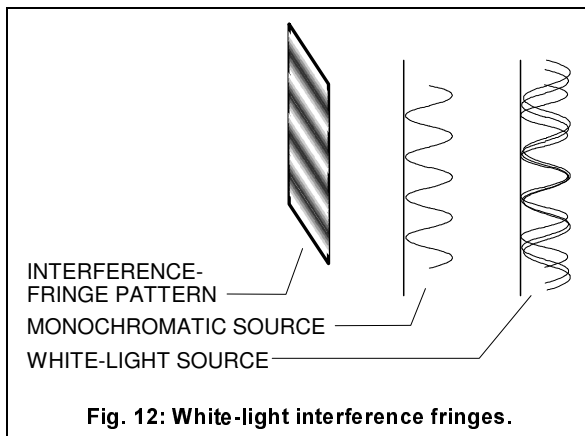
### 3.3 Interference of Monochromatic and White Light

We have thus far assumed that both interfering light beams are perfectly monochromatic and of precisely the same wavelength,  $\lambda_0$ , a condition that will be approximately met only if they have a common source, and this source is a laser running in a single longitudinal mode, in which case interference patterns will remain observable even for very large phase differences,  $\Delta\phi$ .

Beams from broadband sources do not meet this condition, and beams from "white-light" sources do not even come close to meeting it. Substituting Eq. 8 into Eq. 16, we obtain the phase difference,  $\Delta\phi$ , of two interfering beams as a function of their wavelength,  $\lambda_0$

$$\Delta\phi = 2\pi \cdot \frac{n}{\lambda_0} \cdot (z_a - z_b) = 2\pi \cdot \frac{n}{\lambda_0} \cdot \Delta z, \quad (18)$$

which implies that their phase differences vary with wavelength,  $\lambda_0$ , for a given path difference,  $\Delta z$ . Fig. 12 depicts the interference pattern resulting from superimposing two beams composed of three differing wave-

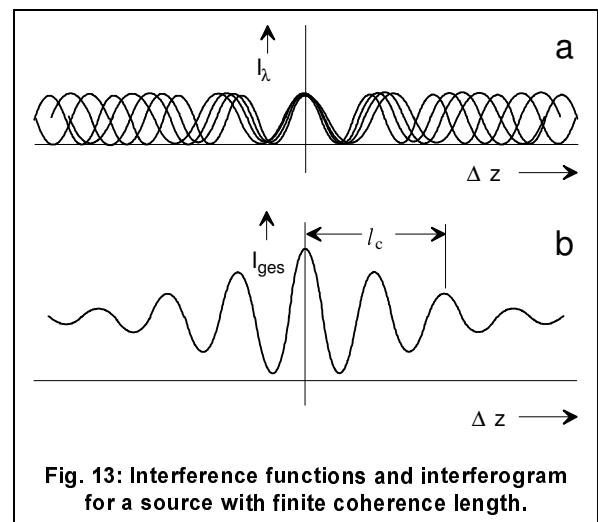


**Fig. 12: White-light interference fringes.**

lengths. Their interference functions appear as fringes of differing spacings when viewed on a screen. Only at the central point, where  $\Delta z = 0$ , and therefore  $\Delta\phi = 0$  for all wavelengths, will an intensity maximum, i.e., a "white-light" interference maximum, occur for all three wavelengths. As  $\Delta z$  increases, the interference functions for the three wavelengths become increasingly out of phase, and the fringe pattern appears dispersed into its spectral components. For large values of  $\Delta z$ , pattern intensity approaches a constant value as the degree of beam interference declines, and the characteristic interference pattern becomes increasingly degraded, finally fading and disappearing altogether.

An identical situation may be observed if the interference of accurately parallel beams, which will thus have the perfectly uniform transverse intensity distributions assumed in Section 3.1, are analyzed by using a detector to measure total incident intensity, i.e., if all wavelength components are measured simultaneously, rather than by studying interference fringes. Fig. 13 shows that in this case as well, interference effects decline with increasing path difference,  $\Delta z$ , due to the growing phase differences,  $\Delta\phi$ , among the three spectral components shown in Fig. 13a.

The value of  $\Delta z$  for which the modulated portion of the resultant interference function, i.e., the interferogram, or, equivalently, its fringe contrast or fringe visibility, drops to half its peak value is defined as the light source's coherence length,  $l_c$  (cf. Fig. 13b). This drop will be more rapid for sources with short coherence lengths, i.e., sources with broad emission spectra. Light sources with long coherence lengths, such as single-longitudinal-mode lasers, will thus be required where large path differences are involved. In many cases measurements are intentionally restricted to small path differences,  $\Delta z$ , an approach that allows using low-coherence light sources, and is thus termed "white-light interferometry."



**Fig. 13: Interference functions and interferogram for a source with finite coherence length.**



Looking at this another way, a two-beam interferometer designed to provide accurately controlled path differences represents an extremely sensitive instrument for analyzing the spectral characteristics of light sources. This is the basic principle underlying Fourier-transform spectroscopy.

## 4 Optical Interferometers

### 4.1 Mach-Zehnder and Michelson Interferometers

In Section 3.1, interference phenomena were discussed for the type of arrangement termed a "Mach-Zehnder" interferometer, a highly symmetric arrangement where both beam paths have virtually identical lengths, i.e.,  $\Delta z = 0$ , for which the effects mentioned in Section 3.3 in conjunction with broadband light sources play a subordinate role. Mach-Zehnder interferometers are incapable of accommodating large values of  $\Delta z$ .

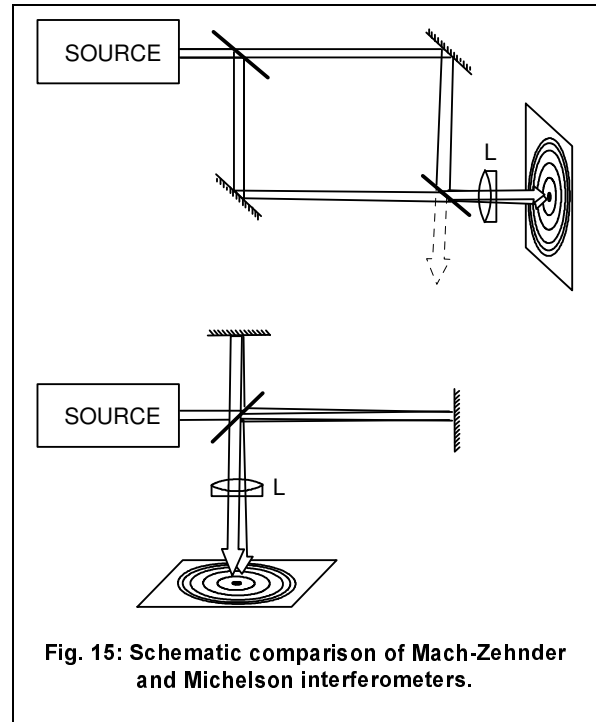
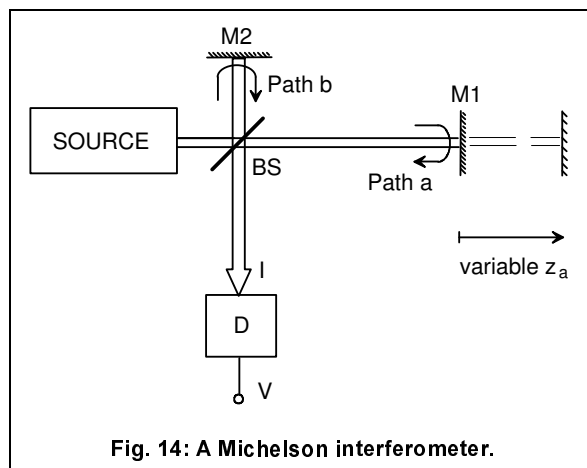
However, we would also like to be able to assemble interferometers capable of accommodating large path differences,  $\Delta z$ , whenever necessary. In such cases, we may use the Michelson-type interferometer shown in Fig. 14, where two-beam interference is implemented by recombining beams retroreflected by two high-reflectance mirrors, M1 and M2, on the same beamsplitter, BS, that initially split the beam from the source. Each beam thus traverses the full length,  $z_a$  or  $z_b$ , of its respective arm twice. The phases of these two beams upon their return to the beamsplitter will thus be given by

$$\phi_a = 2 \cdot 2\pi \cdot \frac{n}{\lambda_0} \cdot z_a, \quad (19a)$$

$$\phi_b = 2 \cdot 2\pi \cdot \frac{n}{\lambda_0} \cdot z_b, \quad (19b)$$

and their relative phase, or phase shift, will be

$$\Delta\phi = 2 \cdot 2\pi \cdot \frac{n}{\lambda_0} \cdot (z_a - z_b). \quad (20)$$

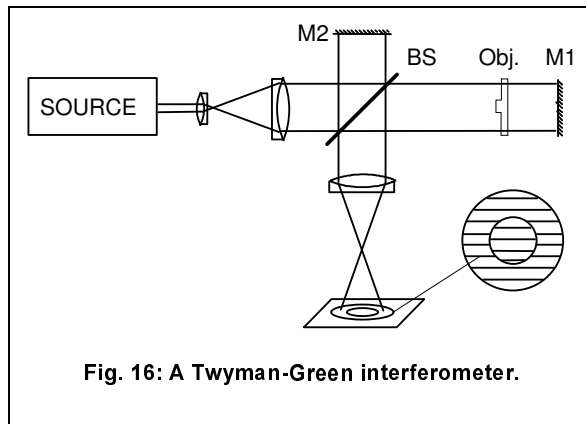


Altering the length of either arm of a Michelson interferometer thus alters the optical pathlength traversed by its beam by twice the change in arm length, i.e., alters its beam's phase by an amount twice that for Mach-Zehnder interferometers. This ability of Michelson interferometers to accommodate large path differences is counteracted by the fact that one of the interfering beams is retroreflected, or fed back, to the source. A major proportion of source intensity is thus unavailable for interferometric analyses, and, even worse, feedback effects may adversely affect source operation and stability.

Mach-Zehnder and Michelson interferometers are further compared in Fig. 15, which also shows their interference-ring patterns. The schematic configurations of Figs. 4 and 14 have here been supplemented by the field lenses, L, needed to project their interference-ring patterns onto the planes of viewing screens.

### 4.2 Michelson and Twyman-Green Interferometers

For the types of interferometers discussed thus far, the objective has been converting pathlength variations,  $\Delta z$ , into measurable intensity variations,  $I(\Delta z)$ . Producing nonuniform lateral intensity distributions in the form of interference fringes or rings is, at best, an aid to better converting quantities to be measured into observable effects. Note that the signs of phase shifts are also immediately recognizable from interference-fringe patterns, which will not be the case for the uniform lateral beam-intensity distributions considered in Section 3.1, where the fundamental factor of interest was the "mean" phase of interfering beams.



The Twyman-Green interferometers to be discussed in this subsection alter this situation. They respond to lateral phase-shift variations, which is why they are employed for, e.g., determining the surface figures and imaging aberrations of optical components. As can be seen from Fig. 16, this configuration is a derivative of the Michelson interferometer obtained by expanding and collimating the beam from the source ahead of the beamsplitter, BS. If both beam paths were optically perfect, i.e., if they incorporated nothing that might cause wavefront distortions, then the two interfering beams would yield the idealized interference-fringe pattern shown in Fig. 16, and the interferometer would respond exclusively to shifts in the positions of one or both of the two mirrors, M1/M2.

This will no longer be the case if a transparent wavefront-distorting object is inserted into one of the beam paths, as shown in Fig. 16, where we have used a "hat"-shaped stepped glass plate in order to simplify explanation. In this case, the interference-fringe pattern projected on the viewing screen will consist of two subpatterns, a circular inner fringe pattern corresponding to the longer optical path through the glass plate's central step, surrounded by an annular fringe pattern corresponding to the shorter

optical path through its thinner periphery. Note that the beam reflected by mirror M1 passes through the object twice, since Twyman-Green interferometers remain essentially Michelson interferometers. In actual practice, there would be little interest in studying such intentionally introduced wavefront distortions. Twyman-Green interferometers are used for, e.g., checking nominally flat optical components for departures from planarity. Further applications include checking spherical mirrors or simple/compound lenses for imaging aberrations. In the latter types of applications, mirror M1 is replaced by a spherical mirror whose center of curvature coincides with the focal point of the mirror or lens being checked, forming a so-called "confocal" optical system.

## 5 Application Notes

### 5.1 Assembling the Experimentation Kit

The interferometer experimentation kit is assembled on a breadboard, and is designed to allow readily configuring the various types of interferometer. Fig. 17 depicts a fully assembled interferometer, complete with all components, that may be readily reconfigured to obtain the various interferometertypes by removing or relocating individual component items.

The experimentation kit lacks a light source, which is to be supplied by users. Recommended is the Linos Photonics 30-1 Modular He-Ne Alignment Laser included with the Linos Photonics 30-1 Laser Kit (Part No. 06 4015). This kit also includes beam-deflecting/beam-expansion optics.

**We expressly caution users that applicable laser-safety regulations should be observed at all times. He-Ne lasers capable of emitting output powers in excess of 1 mW fall under Laser Safety Class 3 B as defined in IEC 825.**

## 5.2 Simple Experiments with the Michelson Interferometer

### 5.2.1 Initial Alignment

The modifications required to convert the basic configuration of Fig. 17 into a Michelson interferometer are schematized in Fig. 18, where unused components are indicated by thin lines. We recommend that users spend time familiarizing themselves with the effects of the alignments of mirrors S1' and S2' on interference effects and the behaviour of interference fringes/rings before proceeding.

The initial step is aligning the horizontal beam path shown in Fig. 18 by blocking kinematic mirror M2' with a piece of black cardboard and adjusting the vertical and horizontal tilt of primary beamsplitter BS1 until the reflected beam from mirror M1' is accurately centered on mirror M2. Insert the white alignment target supplied into the entrance aperture of M2 to verify that the beam is accurately centered on M2. Once this initial step has been concluded, remove the alignment target from M2 and insert it into the entrance aperture on the mount holding the beamsplitter, BS2, shown at the lower right in Fig. 18. Align M2 until the beam is centered on the alignment target, remove the alignment target from BS2, reinsert the target in the entrance aperture of mirror M2, block the

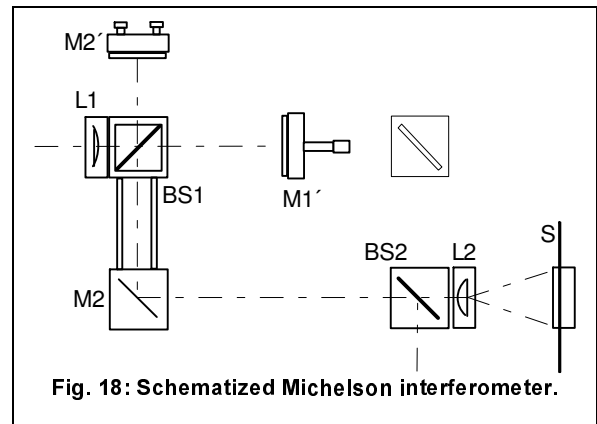


Fig. 18: Schematized Michelson interferometer.

path of the horizontal beam, and align M2' until the vertical beam is centered on M2.

Once these initial alignment procedures have been completed, fine-align mirror M2' until the interfering beams are accurately coaxial and fringe contrast is maximized. The effects of altering the relative phases of the interfering beams may now be demonstrated by longitudinally translating mirror M1' using its micrometer drive. The effects of inserting plano-convex lens L1 may also be studied. With L1 removed, both interfering beams will be highly collimated, i.e., will have roughly planar wavefronts at all points along their respective paths, and their

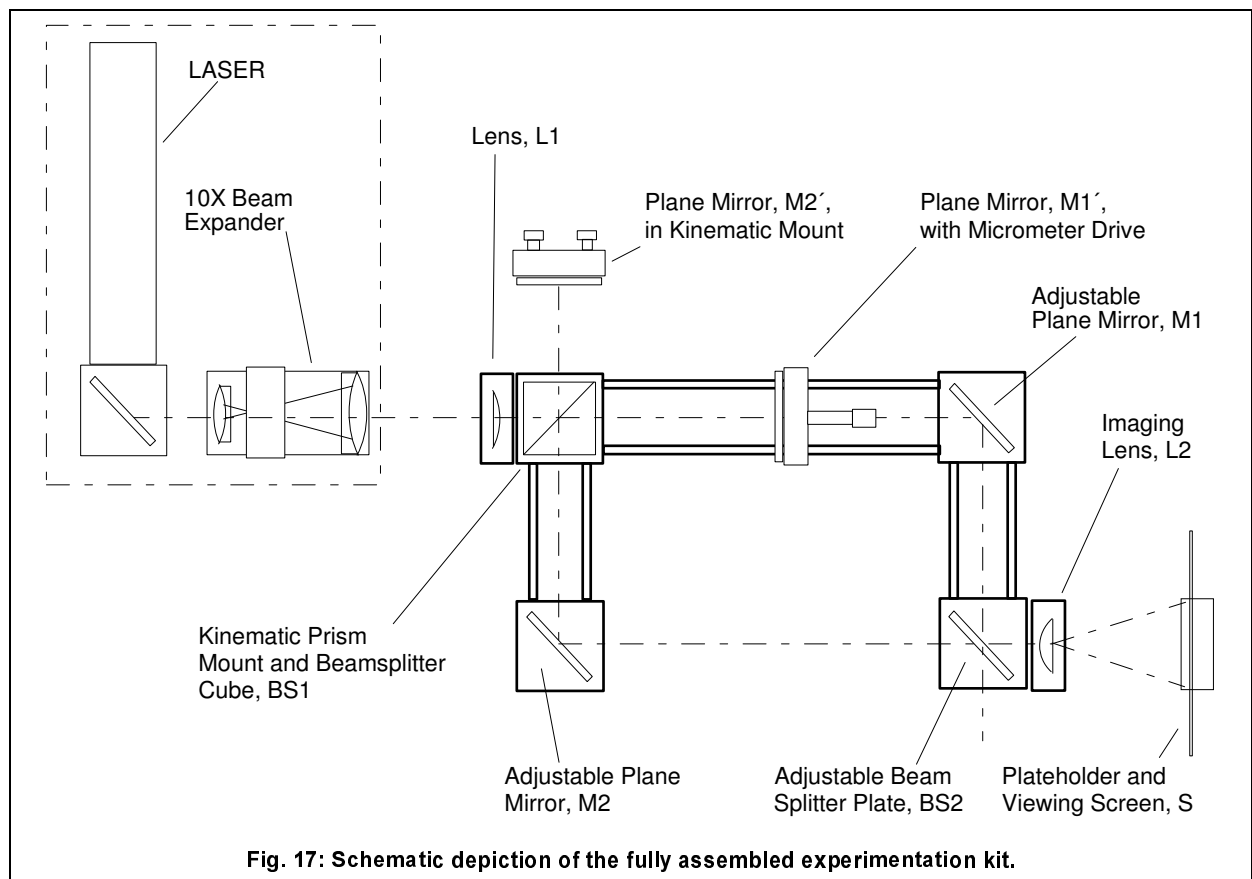
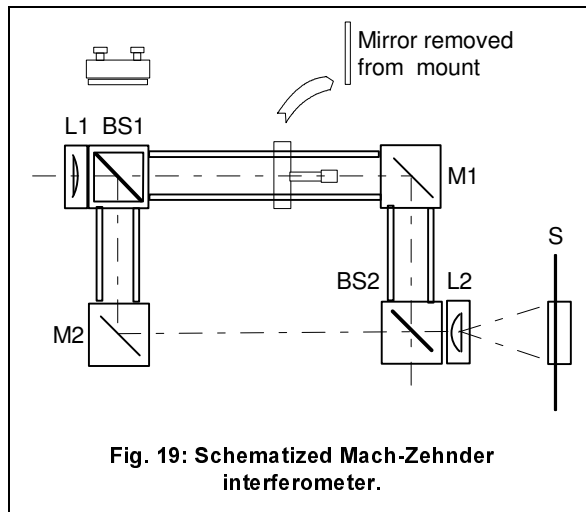


Fig. 17: Schematic depiction of the fully assembled experimentation kit.



interference patterns will thus consist of parallel fringes. Inserting L1 transforms these planar wavefronts into spherical wavefronts, and their interference patterns will then become concentric rings.

Field lens, L2, which projects interference patterns on screen S, may also be mounted on the exit aperture of the mount holding mirror M2. This will allow inserting S between M2 and BS2, where interference-fringes/rings are twice as bright.

An alternative initial alignment procedure involves inserting the alignment target provided into the entrance aperture of BS1. The alignment-target's central aperture will then be imaged as two small-diameter, bright, spots on viewing screen S. Rough-align all optical components of both arms following the procedures stated above until these two spots coincide and are centered on S, and then repeat the fine-alignment procedure described above.

### 5.2.2 Interferometric Studies of the Thermal Expansion of Test Samples

The experimentation kit includes an 80-mm length of 10-mm-diameter steel rod specially prepared for use in thermal-expansion studies. Mount the end of the rod with the longer machined collar in the 10-mm reduction ring supplied with the kit, mount the 10-mm-diameter plane mirror from the kit on the other end of the rod using double-sided adhesive tape or model-airplane cement, install the reduction ring in the kinematic mount, replacing mirror M1', with the mirror on the end of the rod facing the light source, and align the mirror. This steel rod has a drilled hole accepting 4-mm-diameter banana plugs near each end. Connect the rod to a suitable power supply, apply a voltage across the terminals at its ends, and interferometrically determine changes in its length with temperature as Joule-heating rates are varied.

## 5.3 Mach-Zehnder Interferometers

### 5.3.1 Conversion to a Mach-Zehnder Interferometer

Fig. 19 schematically depicts the modifications required to transform the basic experimental setup into a Mach-Zehnder interferometer. Note that all three upper arms are assembled on rods, while the lower arm, that extending from M2 to BS2, has been intentionally left open in order to leave space free for inserting objects to be tested.

Here again, initial alignment involves blocking one of the interfering beams and using the alignment target provided to center the other beam on optical components, proceeding along the optical train from source to viewing screen. It will be best to start by blocking the lower beam and aligning the light source and upper beam path, BS1-M1-BS2. Adjust the height of the light source to vertically center the beam on BS2. Roughly laterally center the beam on BS2 by horizontally repositioning the light source, and conclude by using the alignment adjustments on M1 to laterally center the beam on BS2. Repeat these procedures until the upper beam is accurately centered on the entrance aperture of beamsplitter BS2.

Then block the upper beam and align the lower beam path, BS1-M2-BS2, by first adjusting BS1 to center the beam on M2, and then adjusting M2 to center the beam on BS2.

Unblock the upper beam to allow both beams to fall on BS2. If alignment has been correctly performed, interference fringes should now be visible on screen S. Fringes will usually initially be very narrowly spaced, so be careful not to overlook them. Realign BS1, which offers the best alignment facilities, to maximize fringe visibility.

The roughly equal lengths of both beam paths and expanded beam result in parallel interference fringes rather than concentric rings. Here as well, alignment may alternatively be performed by placing the alignment target on BS1, and following the procedures of the final paragraph of Section 5.2.1.

Mach-Zehnder interferometers are suitable for use in a variety of applications, such as:

- checking the optical quality of glass slides and other optical components,
- studying the effects of temperature changes on transparent objects, and
- determining variations in the refractive indices of gases with pressure.

### 5.3.2 Determining Refractive Indices with a Mach-Zehnder Interferometer

A setup suitable for the latter task is schematically depicted in Fig. 20. A gas cell equipped with two lines, one of which is connected to an open-tube mercury manometer and the other of which is connected to a vacuum pump and a buffer tank used to vent the system, is inserted into one arm. This type of setup will allow determining the refractive index of air as a function of pressure,  $n_A(p)$ , corrected for air temperature.

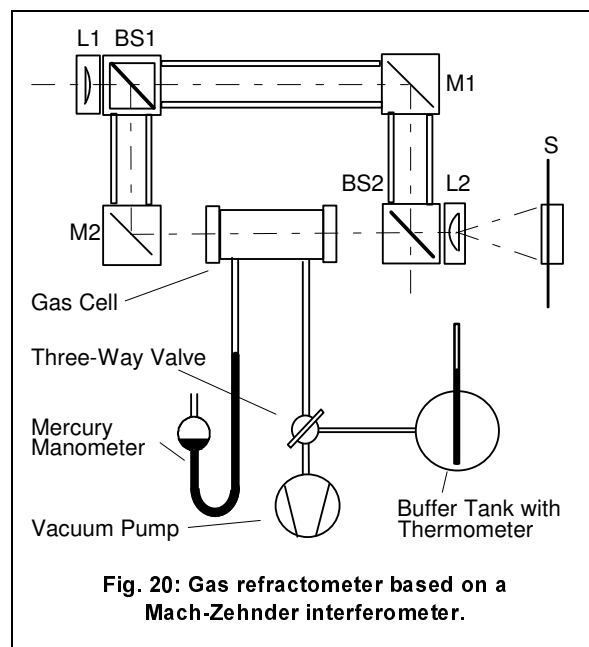
It is worth repetition at this point that the roughly equal beam paths of Mach-Zehnder interferometers allows ready employment of light sources, such as incandescent lamps equipped with line filters, spectral lamps, LED's, etc., with relatively short coherence lengths. Although use of a laser is not absolutely essential, it results in less stringent alignment requirements and brighter interference fringes.

### 5.4 Checking Glass Slides with a Twyman-Green Interferometer

Applications of Twyman-Green interferometers to detection of wavefront distortions have been briefly described in Section 4.3, above. These types of applications are mentioned here once again solely for the sake of completeness, since they will not be discussed further. Use of CCD-cameras, and, if needed, digital image-processing systems, is advisable in these types of applications. Detailed treatments of various methods for analyzing interferograms to determine imaging aberrations of simple lenses, compound lenses, and mirrors will be found in the literature.

## 6 Bibliography

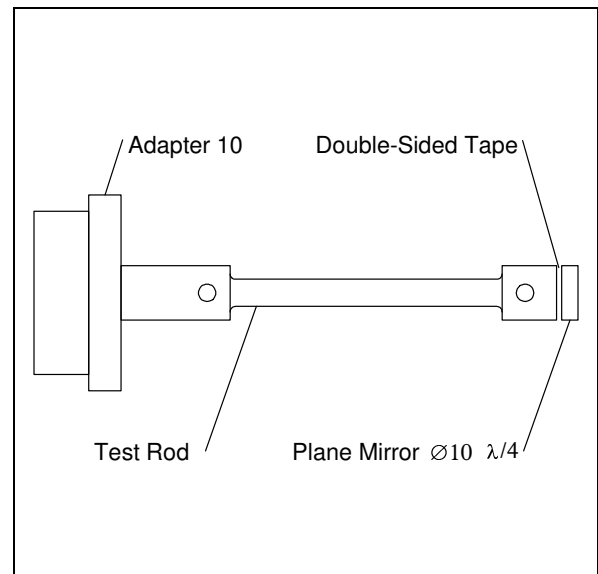
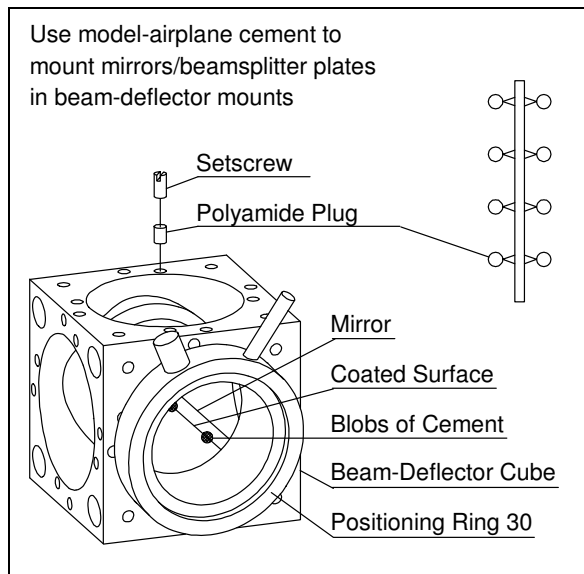
1. P. Hariharan: *Basics of Interferometry*. Academic Press, San Diego and London (1992).
2. P. Hariharan: *Optical Interferometry*. Academic Press, San Diego and London (1985).
3. W. H. Steel: *Interferometry*. Cambridge University Press (1983).
4. S. Tolansky: *An Introduction to Interferometry*. Longman, London (1955).
5. D. Malacara: *Optical Shop Testing*. John Wiley & Sons, New York and Chichester (1978).
6. E. R. Robertson (ed.): *The Engineering Uses of Coherent Optics*. Cambridge University Press (1976).
7. A. C. Hewson: *An Introduction to the Theory of Electromagnetic Waves*. Longman, London (1970).
8. Grant R. Fowles: *Introduction to Modern Optics*. Second edition. Holt, Rinehart and Winston, New York (1975).
9. M. Born and E. Wolf: *Principles of Optics*. Fifth edition. Pergamon Press, Oxford and New York (1980).



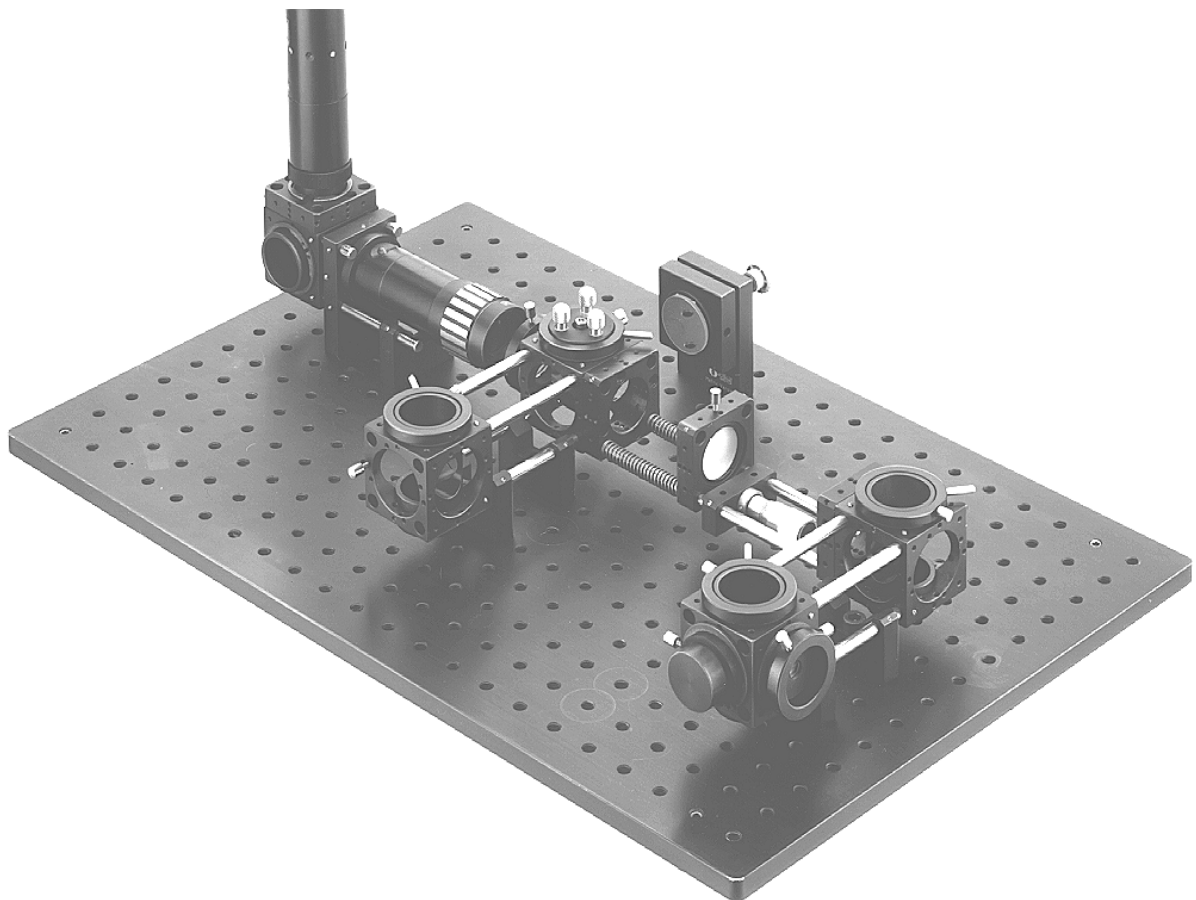
**Fig. 20: Gas refractometer based on a Mach-Zehnder interferometer.**

## 7 Assembly Drawings and Photographs

### 7.1 Component Modules

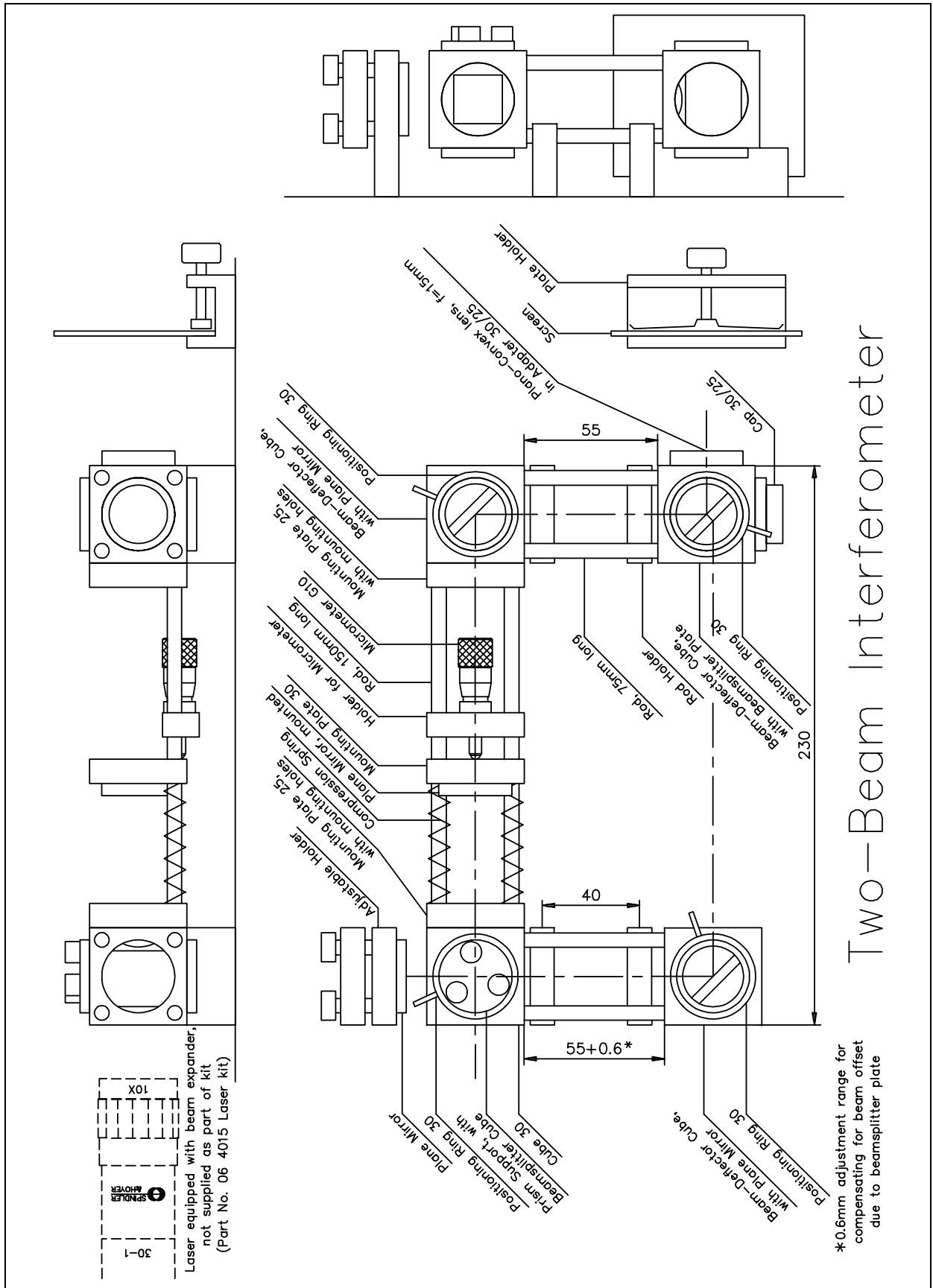


### 7.2 Photograph of the Fully Assembled Two-Beam Interferometer

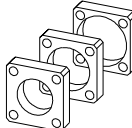





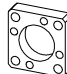





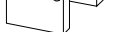


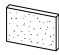


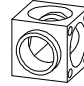


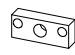

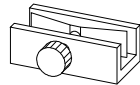







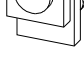



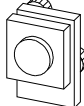




7.3 Assembly Drawing



## 8 Components List

Designation	Part No.	Qty.	Designation	Part No.	Qty.
 Mounting Plate 35	06 1047		 Plane Mirror, 25 mm, $\lambda/2$ , mounted	06 4010 901	1
 Mounting Plate 30	06 1042	1	 Mount CL 25.4	06 3663	1
 Mounting Plate 25	06 1010		 Compression Spring, 60x8x0.7	06 1159	2
 Mounting Plate 25 with mounting holes	06 1041	2	 Micrometer G10	06 1162	1
 Rod Holder F	06 1227	4	 Adapter 10	06 4010 031	1
 Rod Holder G	06 1229		 Test Rod	06 4010 030	1
 Rod Holder	06 1228		 Beamsplitter Cube, 20x20x20	33 5520	1
 Cube 30	06 1081	1	 Beamsplitter Plate, 20x30x2.5	34 4143	1
 Cube 25	06 1080		 Plane Mirror, 20x30x2.5	34 0060	2
 Beam Deflector Cube	06 1084	3	 Positioning Ring 30	06 5092	4
 Rod, 75 mm long	06 1209	8	 Holder for Micrometer G10	06 1160	1
 Rod, 150 mm long	06 1210	2	 Plate Holder	03 6028	1
 Plano-Convex Lens $f=15$ mm	06 3039	1	 Cap 30/25	06 1601	1
 Plano-Convex Lens $f=150$ mm	06 3048	1	 Mounting Plate 460x300	06 1313	1
 Plane Mirror, 25.4 mm, $\lambda/2$	34 0085	1	 Assembly Kit		
 Plane Mirror, 10 mm, $\lambda/4$	34 0081	1	 Tool Kit		
 Adapter 30/25	06 1602	2	 Laboratory Manual	06 4010 059	1
 Prism Support 30	06 5085	1			
 Mirror Mount	03 6098	1			